Nonlinear effects resulting from the interaction of a large-scale Alfvén wave with a density filament

T. Drozdenko and G. J. Morales[a)]
Department of Physics and Astronomy, University of California at Los Angeles, Los Angeles, California 90095

(Received 28 November 2000; accepted 10 April 2001)

This analytic study investigates the nonlinear plasma response when a shear Alfvén wave of large transverse scale interacts with a field-aligned density perturbation whose transverse scale is comparable to the electron skin depth. The interaction between the large-scale wave and the density perturbation produces a small-scale shear mode [T. Drozdenko and G. J. Morales, Phys. Plasmas **7**, 823 (2000)], which facilitates the transfer of energy to the plasma particles. The beat of the large-scale wave with the small-scale wave can lead to ponderomotive forces and flows in the plasma, or, if the field amplitudes of the small-scale wave are large enough to produce oscillatory velocities comparable to the electron thermal velocity, a streaming instability may develop. In this study, it is demonstrated that nonlinear effects arise in regions remote from the seed perturbation, and estimates of the amplitude of the large-scale wave necessary to produce significant ponderomotive density changes or trigger significant streaming instabilities are presented. © *2001 American Institute of Physics.* [DOI: 10.1063/1.1376652]

I. INTRODUCTION

In several areas of contemporary plasma research[1–4] there is a strong interest in identifying a means of transferring the energy stored in large-scale Alfvén waves to the plasma particles. This issue is nontrivial because effective interactions with plasma particles require significant parallel electric fields, sharp amplitude gradients, or a combination of the two. But, both of these features are negligible for the large-scale waves which initially act as the energy reservoir in many applications. A specific example of this energy transfer scenario has recently been identified in high-resolution measurements[5] made by the POLAR spacecraft traveling through the plasma-sheet boundary layer in the earth's magnetosphere (at altitudes of 4–6 Earth radii). The POLAR observations are able to correlate the presence of large-scale Alfvén waves with the development of microscopic Alfvén waves (i.e., having transverse scale on the order of the electron skin depth), and the generation of energetic electrons and heated ions. These wave features have been simultaneously identified with optical signatures of the aurora at lower altitudes.

From a theoretical perspective, one can roughly identify several stages that contribute to the ultimate relaxation of the energy stored in large-scale Alfvén waves. First, a mechanism must operate that causes a transformation of the spatial scale transverse to the confining magnetic field. For the case of interest in this study, i.e., low-β plasmas, this corresponds to secondary waves with scales on the order of the electron skin depth. A second stage arises in which the parallel electric fields and amplitude gradients associated with the beat of the large-scale mode with the secondary wave results in nonlinear effects. Eventually, the nonlinear effects cause particle acceleration, density modifications, flows, and high-frequency noise. A very interesting late stage (but yet poorly understood) follows in which the plasma spontaneously develops long-lived structures consisting of density and temperature channels. Such structures have been shown[6,7] to act as spontaneous generators of drift-Alfvénic turbulence that results in enhanced transport of the ambient plasma.

In a previous analytical study,[8] we investigated the properties of a specific scale-transformation scenario presented pictorially in Fig. 1. It consists of the interaction between a shear Alfvén wave propagating along the confining magnetic field (i.e., with $k_\perp = 0$) and an ambient, field-aligned, filamentary density perturbation with small transverse scale. The fractional density perturbation level $\delta n/n_0$ is envisioned to be in the range of 1%–10%. The polarization velocity, induced by the large-scale wave on the plasma ions, beats with the density perturbation to produce an *in situ* source with an azimuthal dependence about the confining magnetic field. This effective antenna radiates forward and backward shear Alfvén waves of small transverse scale that develop parallel electric fields. The amplitude of the secondary waves is proportional to $\delta n/n_0$ and depends linearly on the amplitude of the large-scale wave. The efficiency of the transformation process has been summarized by an effective scattering cross section. The three-dimensional topology of the process consists of two self-consistent, field-aligned current filaments of opposite polarity. As the dipolar current filaments propagate away from the source, they exhibit a radial spreading that is bounded by the cone trajectories[9–11] associated with inertial Alfvén waves of small transverse scale.

The present study addresses issues related to the second stage of the overall relaxation scheme previously outlined.

a)Electronic mail: morales@physics.ucla.edu

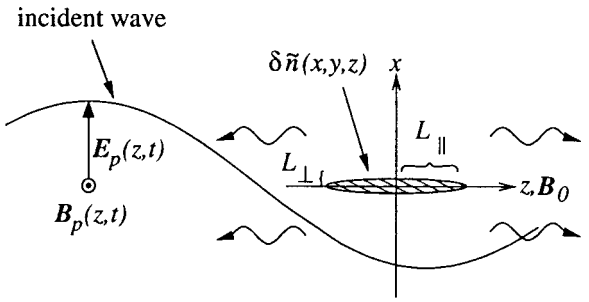

FIG. 1. Schematic of a large-scale Alfvén wave of frequency ω (with $k_\perp = 0$) incident on a field-aligned density perturbation with axial and transverse scale lengths $L_\parallel$ and $L_\perp$, where $L_\parallel \gg L_\perp$ and $L_\perp$ is on the order of the electron skin depth. The interaction gives rise to right- and left-going collimated shear waves with finite parallel electric fields.

We consider two manifestations of nonlinear effects that can result from the scale transformation scenario analyzed in Ref. 8. At intermediate amplitude levels, time-averaged ponderomotive forces arise while under extreme conditions the parallel electric field becomes sufficiently large, so that electron–ion streaming instabilities are triggered. In this work, we identify the relevant ponderomotive effects, namely the parallel dc force and associated transverse flows. It is found that the overwhelming ponderomotive effects arise from the beat of the primary (pump) wave with the backscattered short-scale wave. To complement the ponderomotive study, we also assess the spatial growth of streaming instabilities associated with the parallel velocity imparted to the electrons during the transformation process.

The manuscript is organized as follows: Section II explores the general ponderomotive force acting on a plasma and the resulting dc drift velocities in the limit of a cold-fluid plasma. No assumption about the topology of the electric and magnetic fields is made. In Sec. III, the specific field topology calculated in Ref. 8 is applied to the general results found in Sec. II. In Sec. IV, streaming instabilities arising from the acceleration of electrons in the parallel direction are examined. Conclusions are presented in Sec. V.

II. PONDEROMOTIVE FORCES IN THE LOW-β LIMIT

This section evaluates the general time-averaged fluid force (i.e., the ponderomotive force) associated with a shear-Alfvén-type field structure in a cold plasma, as is relevant for conditions in which the electron plasma-β satisfies $\beta_e \ll 2m/M$, where m and M are the electron and ion mass, respectively.

The cold fluid equation of motion for species α having charge q_α, mass m_α, density n_α, and velocity v_α is given by

$$n_\alpha m_\alpha \left[\frac{\partial \mathbf{v}_\alpha}{\partial t} + \mathbf{v}_\alpha \cdot \nabla \mathbf{v}_\alpha\right] = n_\alpha q_\alpha \mathbf{E} + n_\alpha \frac{q_\alpha}{c} \mathbf{v}_\alpha \times (\mathbf{B} + B_0 \hat{\mathbf{z}}), \tag{1}$$

where B_0 is the strength of the static confining magnetic field aligned with the z direction of the Cartesian coordinate system (x,y,z).

For modest levels of nonlinearity, it is assumed that in zeroth order the electric and magnetic fields of the shear Alfvén structure are well represented by a harmonic (monochromatic) time dependence at frequency ω having the form

$$\mathbf{E} = \tilde{\mathbf{E}} e^{-i\omega t} + \text{c.c.}, \tag{2}$$

$$\mathbf{B} = \tilde{\mathbf{B}} e^{-i\omega t} + \text{c.c.}, \tag{3}$$

in which the complex vector amplitudes $(\tilde{\mathbf{E}}, \tilde{\mathbf{B}})$ in general depend on (x,y,z), i.e., we envision a three-dimensional situation, as is appropriate for the scale transformation process considered in Ref. 8. At this stage, we do not assume specific functional forms for $(\tilde{\mathbf{E}}, \tilde{\mathbf{B}})$, but, in Sec. III, numerical results are presented that examine the behavior resulting from the more involved fields associated with the interaction of a large-scale propagating Alfvén wave with a filamentary density perturbation.

As is common in calculations of ponderomotive forces, it is assumed that the oscillatory fields $(\mathbf{E},\mathbf{B})$ cause, to first order, an oscillatory velocity

$$\mathbf{v}_\alpha^{(1)} = \tilde{\mathbf{v}}_\alpha \mathbf{e}^{-\mathbf{i}\omega\mathbf{t}} + \text{c.c.}, \tag{4}$$

in which $\tilde{\mathbf{v}}_\alpha$ also depends on (x,y,z) and is given by

$$\tilde{\mathbf{v}}_\alpha = \frac{c}{B_0}\left[\underset{\tilde{\mathbf{v}}_\mathbf{p}}{\pm \frac{i\omega\Omega_\alpha}{(\omega^2-\Omega_\alpha^2)}\tilde{\mathbf{E}}_\perp} \underset{\tilde{\mathbf{v}}_{E\times B}}{- \frac{\Omega_\alpha^2}{(\omega^2-\Omega_\alpha^2)}(\tilde{\mathbf{E}}_\perp \times \hat{\mathbf{z}})} \underset{\tilde{\mathbf{v}}_z}{\pm i\frac{\Omega_\alpha}{\omega}\tilde{E}_\parallel \hat{\mathbf{z}}}\right], \tag{5}$$

where c is the speed of light and Ω_α is the gyrofrequency of species α (a positive quantity). The $(\pm)$ signs refer to $(\pm)$ charges, $\tilde{E}_\parallel$ is the electric field component along the confining magnetic field, and $\tilde{E}_\perp$ is the transverse component. The small labels above the different terms in Eq. (5) indicate their physical origin; $\tilde{\mathbf{v}}_\mathbf{p}$ refers to the polarization drift, $\tilde{\mathbf{v}}_{E\times B}$ to the $E\times B$ drift, and $\tilde{v}_z$ is the axial jitter. Similar terminology is used later to help identify the origin of more complicated expressions.

The calculation of the fluid ponderomotive force essentially amounts to isolating the zero-frequency components of the driving terms in Eq. (1). To second order in the strength of the oscillatory electric field, the time-averaged force (not the force density) acting on species α is

$$\langle \mathbf{F} \rangle_\alpha = 2\,\text{Re}\left[\frac{q_\alpha}{c}\tilde{\mathbf{v}}_\alpha^* \times \tilde{\mathbf{B}} - m_\alpha (\tilde{\mathbf{v}}_\alpha^* \cdot \nabla)\tilde{\mathbf{v}}_\alpha\right], \tag{6}$$

where Re refers to the real part.

Using Faraday's law to relate $\tilde{\mathbf{B}}$ to $\tilde{\mathbf{E}}$ and the explicit form of Eq. (1) to evaluate the expression in Eq. (6) yields the lengthy expression

$$\langle \mathbf{F} \rangle_\alpha = -m_\alpha \frac{c^2}{B_0^2} \left\{ \frac{\Omega_\alpha^2(\omega^2+\Omega_\alpha^2)}{(\omega^2-\Omega_\alpha^2)^2} \left[\nabla|\tilde{E}_\perp|^2 - \partial_z|\tilde{E}_\perp|^2\hat{\mathbf{z}} \right] + \boxed{-m_\alpha(\tilde{\mathbf{v}}_\mathrm{p}^*\cdot\nabla)\tilde{\mathbf{v}}_\mathrm{p} - m_\alpha(\tilde{\mathbf{v}}_{E\times B}^*\cdot\nabla)\tilde{\mathbf{v}}_{E\times B}} \right.$$

$$+ \frac{\Omega_\alpha^2}{\omega^2}\nabla|\tilde{E}_\parallel|^2 \boxed{-m_\alpha(\tilde{\mathbf{v}}_z^*\cdot\nabla)\tilde{\mathbf{v}}_z}$$

$$+ \frac{\Omega_\alpha^2}{(\omega^2-\Omega_\alpha^2)}\partial_z|\tilde{E}_\perp|^2\hat{\mathbf{z}} - \frac{2\Omega_\alpha^4}{(\omega^2-\Omega_\alpha^2)^2}\,\mathrm{Re}\left[(\nabla\cdot\tilde{\mathbf{E}}_\perp)\tilde{\mathbf{E}}_\perp^* \right] \boxed{q_\alpha\tilde{\mathbf{v}}_\mathrm{p}^*\times\tilde{\mathbf{B}}/c - m_\alpha(\tilde{\mathbf{v}}_\mathrm{p}^*\cdot\nabla)\tilde{\mathbf{v}}_z - m_\alpha(\tilde{\mathbf{v}}_z^*\cdot\nabla)\tilde{\mathbf{v}}_\mathrm{p}} \boxed{-m_\alpha(\tilde{\mathbf{v}}_{E\times B}^*\cdot\nabla)\tilde{\mathbf{v}}_{E\times B}}$$

$$- \frac{2\Omega_\alpha^4}{\omega^2(\omega^2-\Omega_\alpha^2)}\,\mathrm{Re}\left[(\tilde{E}_\parallel^*\hat{\mathbf{z}})\times(\nabla\times\tilde{\mathbf{E}}_\perp) \right] \boxed{q_\alpha\tilde{\mathbf{v}}_z^*\times\tilde{\mathbf{B}}/c - m_\alpha(\tilde{\mathbf{v}}_\mathrm{p}^*\cdot\nabla)\tilde{\mathbf{v}}_z - m_\alpha(\tilde{\mathbf{v}}_z^*\cdot\nabla)\tilde{\mathbf{v}}_\mathrm{p}}$$

$$\mp \frac{2\Omega_\alpha^3}{\omega(\omega^2-\Omega_\alpha^2)}\,\mathrm{Im}\left[\tilde{\mathbf{E}}_\perp^*\cdot(\nabla\times\tilde{\mathbf{E}}_\perp)\hat{\mathbf{z}} + (\tilde{E}_\parallel^*\hat{\mathbf{z}})\times\partial_z\tilde{\mathbf{E}}_\perp \right] \boxed{q_\alpha\tilde{\mathbf{v}}_{E\times B}^*\times\tilde{\mathbf{B}}/c - m_\alpha(\tilde{\mathbf{v}}_{E\times B}^*\cdot\nabla)\tilde{\mathbf{v}}_z - m_\alpha(\tilde{\mathbf{v}}_z^*\cdot\nabla)\tilde{\mathbf{v}}_{E\times B}}$$

$$\mp \frac{2\omega\Omega_\alpha^3}{(\omega^2-\Omega_\alpha^2)^2}\,\mathrm{Im}\left[\nabla(\tilde{\mathbf{E}}_\perp^*\cdot(\tilde{\mathbf{E}}_\perp\times\hat{\mathbf{z}})) + \tilde{\mathbf{E}}_\perp^*\cdot(\nabla\times\tilde{\mathbf{E}}_\perp)\hat{\mathbf{z}} \right. \boxed{-m_\alpha(\tilde{\mathbf{v}}_{E\times B}^*\cdot\nabla)\tilde{\mathbf{v}}_\mathrm{p} - m_\alpha(\tilde{\mathbf{v}}_\mathrm{p}^*\cdot\nabla)\tilde{\mathbf{v}}_{E\times B}}$$

$$\left. \left. + \tilde{\mathbf{E}}_\perp^*\times(\nabla\cdot\tilde{\mathbf{E}}_\perp\hat{\mathbf{z}}) + \tilde{\mathbf{E}}_\perp\times\partial_z\tilde{\mathbf{E}}_\perp^* \right] \right\}, \tag{7}$$

in which the origin of each term is indicated by a small boxed expression above it, and Re and Im refer to the real and imaginary parts, respectively.

Since the axial component of the ponderomotive force plays an important role in the modification of the ambient plasma density and has been the subject of recent[12,13] studies and controversy,[14] it is useful to write down the parallel component separately. In the cold plasma limit, this term takes the form

$$\langle F \rangle_{\alpha z} = -m_\alpha \frac{c^2}{B_0^2} \left\{ \boxed{-m_\alpha(\tilde{\mathbf{v}}_z^*\cdot\nabla)\tilde{\mathbf{v}}_z} \frac{\Omega_\alpha^2}{\omega^2}\partial_z|\tilde{E}_\parallel|^2 + \boxed{q_\alpha\tilde{\mathbf{v}}_\mathrm{p}^*\times\tilde{\mathbf{B}}/c - m_\alpha(\tilde{\mathbf{v}}_\mathrm{p}^*\cdot\nabla)\tilde{\mathbf{v}}_z - m_\alpha(\tilde{\mathbf{v}}_z^*\cdot\nabla)\tilde{\mathbf{v}}_\mathrm{p}} \frac{\Omega_\alpha^2}{(\omega^2-\Omega_\alpha^2)}\partial_z|\tilde{E}_\perp|^2 \right.$$

$$\left. \mp \frac{2\Omega_\alpha^3}{\omega(\omega^2-\Omega_\alpha^2)}\,\mathrm{Im}\left[\tilde{\mathbf{E}}_\perp^*\cdot(\nabla\times\tilde{\mathbf{E}}_\perp) \right] \boxed{q_\alpha\tilde{\mathbf{v}}_{E\times B}^*\times\tilde{\mathbf{B}}/c - m_\alpha(\tilde{\mathbf{v}}_{E\times B}^*\cdot\nabla)\tilde{\mathbf{v}}_z - m_\alpha(\tilde{\mathbf{v}}_z^*\cdot\nabla)\tilde{\mathbf{v}}_{E\times B}} \right\}. \tag{8}$$

In the low-frequency limit ($\omega \ll \Omega_i$) typically associated with shear-Alfvén structures, Eq. (8) becomes

$$\langle F \rangle_{\alpha z} \rightarrow \left\{ \frac{-q_\alpha^2}{m_\alpha\omega^2}\partial_z|\tilde{E}_\parallel|^2 + m_\alpha\frac{c^2}{B_0^2}\partial_z|\tilde{E}_\perp|^2 \right.$$

$$\left. \mp \frac{2q_\alpha c}{\omega B_0}\,\mathrm{Im}[\tilde{\mathbf{E}}_\perp^*\cdot(\nabla\times\tilde{\mathbf{E}}_\perp)] \right\}. \tag{9}$$

The term involving the imaginary part is mass independent, but its direction depends on the sign of the charge. Thus, it does not contribute to the total bulk force acting on the plasma, but the individual species experience a finite effect due to this part of the interaction whose origin is indicated by the boxed expression in Eq. (7). It is also worth noting that contributions from the axial gradients of the parallel and perpendicular field amplitudes have opposite sign. Therefore, conclusions about whether shear Alfvén structures give rise to density depletions or enhancements require appropriate self-consistent evaluations of the field quantities. This is a feature that must be carefully assessed when trying to interpret laboratory[15] and spacecraft observations[16] of density cavities and their relationship to Alfvénic structures.

In the perpendicular direction, the motion of the plasma is constrained by the background magnetic field, thus the perpendicular components of the zero-frequency forces result in perpendicular dc drift velocities given by

$$\mathbf{u}_{\alpha\perp} = \frac{c}{q_\alpha B_0}\langle \mathbf{F} \rangle_\alpha \times \hat{\mathbf{z}}\,. \tag{10}$$

In Sec. III, this expression is evaluated for the self-consistent fields associated with the scale transformation process.

III. PONDEROMOTIVE EFFECTS DUE TO SCALE TRANSFORMATION

Figure 1 provides a useful schematic of the problem considered. It is assumed at this stage that the self-consistent complex amplitudes $\tilde{E}_\perp$, $\tilde{E}_\parallel$ appearing in Eq. (7) are known. In the problem considered, the field quantities contain two terms. One is associated with the primary large-scale wave and the other with the excited small-scale waves whose propagation is bounded by the cone angle given by $\tan\theta_c = (\omega/\Omega_i)\sqrt{m/M}$. As sketched in Fig. 1, one of the small-scale waves propagates along the positive z direction, while the other propagates in the negative z direction. Thus, the counterpropagating wave interferes with the primary wave and creates a partially standing signal located to the left of the ambient density perturbation. In the expressions for the ponderomotive force and flow, those terms that depend on the gradient of a squared amplitude have a larger effect in regions where a partially standing wave forms than in regions where only a traveling wave exists.

The relevant electric and magnetic field amplitudes are given by

$$\tilde{\mathbf{E}} = [E_p e^{i\xi} + E_x(k_s x, k_s y, \xi)]\hat{\mathbf{x}} + E_y(k_s x, k_s y, \xi)\hat{\mathbf{y}} + E_z(k_s x, k_s y, \xi)\hat{\mathbf{z}}, \tag{11}$$

$$\tilde{\mathbf{B}} = B_x(k_s x, k_s y, \xi)\hat{\mathbf{x}} + [B_p e^{i\xi} + B_y(k_s x, k_s y, \xi)]\hat{\mathbf{y}}, \tag{12}$$

where $k_s = \omega_{pe}/c$, $\xi = \omega z/v_A$, and $v_A = B_0/\sqrt{4\pi M n_0}$ is the Alfvén speed of the uniform plasma. M is the ion mass and n_0 is the zeroth-order density of the plasma. In this model, the initial large-scale wave is polarized with its electric field along the x direction. This feature has implications for the interpretation of the figures shown later. In Eqs. (11) and (12), (E_p, B_p) represents the electric and magnetic fields of the large-scale wave while (E_j, B_j) correspond to those of the small-scale signals, which in turn are proportional to the quantity $E_p(\delta n/n_0)$ and are thus much smaller.

The resulting expressions for the components of the ponderomotive force associated with the scale transformation process are

$$\langle F\rangle_{\alpha x} = -m_\alpha \frac{c^2}{B_0^2}\left\{ \frac{\Omega_\alpha^2(\omega^2+\Omega_\alpha^2)}{(\omega^2-\Omega_\alpha^2)^2}[2\,\mathrm{Re}(E_p^* e^{-i\xi}\partial_x E_x) + \partial_x(|E_x|^2+|E_y|^2)] + \frac{\Omega_\alpha^2}{\omega^2}\partial_x|E_z|^2 - \frac{\Omega_\alpha^4}{(\omega^2-\Omega_\alpha^2)^2}[\partial_x|E_x|^2 + 2\,\mathrm{Re}(E_p^* e^{-i\xi}(\partial_x E_x + \partial_y E_y) + E_x^*\partial_y E_y)] + \frac{2\Omega_\alpha^4}{\omega^2(\omega^2-\Omega_\alpha^2)}\mathrm{Re}[E_z\partial_z(E_p^* e^{-i\xi} + E_x^*)] \pm \frac{2\Omega_\alpha^3}{\omega(\omega^2-\Omega_\alpha^2)}\mathrm{Im}[E_z^*\partial_z E_y] \mp \frac{2\omega\Omega_\alpha^3}{(\omega^2-\Omega_\alpha^2)^2}\mathrm{Im}[E_p^* e^{-i\xi}(\partial_x E_y + \partial_y E_x) + \partial_x(E_y E_x^*) + E_x^*\partial_x E_y + E_y^*\partial_y E_y]\right\}, \tag{13}$$

$$\langle F\rangle_{\alpha y} = -m_\alpha \frac{c^2}{B_0^2}\left\{ \frac{\Omega_\alpha^2(\omega^2+\Omega_\alpha^2)}{(\omega^2-\Omega_\alpha^2)^2}[2\,\mathrm{Re}(E_p^* e^{-i\xi}\partial_x E_y) + \partial_y(|E_x|^2+|E_y|^2)] + \frac{\Omega_\alpha^2}{\omega^2}\partial_y|E_z|^2 - \frac{\Omega_\alpha^4}{(\omega^2-\Omega_\alpha^2)^2} \times [\partial_y|E_y|^2 + 2\,\mathrm{Re}(E_y^*\partial_x E_x)] + \frac{2\Omega_\alpha^4}{\omega^2(\omega^2-\Omega_\alpha^2)}\mathrm{Re}[E_z^*\partial_z E_y] \pm \frac{2\Omega_\alpha^3}{\omega(\omega^2-\Omega_\alpha^2)}\mathrm{Im}[E_z\partial_z(E_p^* e^{-i\xi} + E_x^*)] \mp \frac{2\omega\Omega_\alpha^3}{(\omega^2-\Omega_\alpha^2)^2}\mathrm{Im}[E_p^* e^{-i\xi}(\partial_y E_y - \partial_x E_x) + \partial_y(E_y E_x^*) - E_x^*\partial_x E_x - E_y^*\partial_x E_y]\right\}, \tag{14}$$

$$\langle F\rangle_{\alpha z} = -m_\alpha \frac{c^2}{B_0^2}\left\{ \frac{\Omega_\alpha^2}{\omega^2}\partial_z|E_z|^2 + \frac{\Omega_\alpha^2}{(\omega^2-\Omega_\alpha^2)}[2\,\mathrm{Re}(\partial_z(E_p^* e^{-i\xi}E_x)) + \partial_z(|E_x|^2+|E_y|^2)] \pm \frac{2\Omega_\alpha^3}{\omega(\omega^2-\Omega_\alpha^2)}\mathrm{Im}[E_y\partial_z(E_p^* e^{-i\xi} + E_x^*) + (E_p^* e^{-i\xi} + E_x^*)\partial_z E_y]\right\}, \tag{15}$$

and the corresponding components of the dc drift velocity are

$$\langle u\rangle_{\alpha x} = -\frac{c^2}{B_0^2}\left\{ \pm\frac{\Omega_\alpha(\omega^2+\Omega_\alpha^2)}{(\omega^2-\Omega_\alpha^2)^2}[2\,\mathrm{Re}(E_p^* e^{-i\xi}\partial_x E_y) + \partial_y(|E_x|^2+|E_y|^2)] \pm \frac{\Omega_\alpha}{\omega^2}\partial_y|E_z|^2 \mp \frac{\Omega_\alpha^3}{(\omega^2-\Omega_\alpha^2)^2} \times [\partial_y|E_y|^2 + 2\,\mathrm{Re}(E_y^*\partial_x E_x)] \pm \frac{2\Omega_\alpha^3}{\omega^2(\omega^2-\Omega_\alpha^2)}\mathrm{Re}[E_z^*\partial_z E_y] + \frac{2\Omega_\alpha^2}{\omega(\omega^2-\Omega_\alpha^2)}\mathrm{Im}[E_z\partial_z(E_p^* e^{-i\xi} + E_x^*)] - \frac{2\omega\Omega_\alpha^2}{(\omega^2-\Omega_\alpha^2)^2}\mathrm{Im}[E_p^* e^{-i\xi}(\partial_y E_y - \partial_x E_x) + \partial_y(E_y E_x^*) - E_x^*\partial_x E_x - E_y^*\partial_x E_y]\right\}, \tag{16}$$

$$\langle u\rangle_{\alpha y}=\frac{c^2}{B_0^2}\left\{\pm\frac{\Omega_\alpha(\omega^2+\Omega_\alpha^2)}{(\omega^2-\Omega_\alpha^2)^2}[2\,\mathrm{Re}(E_p^* e^{-i\xi}\partial_x E_x)+\partial_x(|E_x|^2+|E_y|^2)]\pm\frac{\Omega_\alpha}{\omega^2}\partial_x|E_z|^2\mp\frac{\Omega_\alpha^3}{(\omega^2-\Omega_\alpha^2)^2}[\partial_x|E_x|^2\right.$$
$$+2\,\mathrm{Re}(E_p^* e^{-i\xi}(\partial_x E_x+\partial_y E_y)+E_x^*\partial_y E_y)]\pm\frac{2\Omega_\alpha^3}{\omega^2(\omega^2-\Omega_\alpha^2)}\mathrm{Re}[E_z\partial_z(E_p^* e^{-i\xi}+E_x^*)]+\frac{2\Omega_\alpha^2}{\omega(\omega^2-\Omega_\alpha^2)}\mathrm{Im}[E_z^*\partial_z E_y]$$
$$\left.-\frac{2\omega\Omega_\alpha^2}{(\omega^2-\Omega_\alpha^2)^2}\mathrm{Im}[E_p^* e^{-i\xi}(\partial_x E_y+\partial_y E_x)+\partial_x(E_y E_x^*)+E_x^*\partial_x E_y+E_y^*\partial_y E_y]\right\}. \tag{17}$$

As mentioned earlier in this section, for terms with the same multiplying factor, the beat terms in Eqs. (13)–(17) dominate the force and flow patterns because they are larger (by a factor of $n_0/\delta n$) than the contribution arising solely from the small-scale fields.

In the low-frequency limit, as is appropriate for a shear Alfvén structure, the largest terms of the components of the ponderomotive force and drift velocity experienced by the electrons are

$$\langle F\rangle_{ex}\rightarrow 2m\left(\frac{M}{m}\right)^2\left(\frac{c}{B_0}\frac{\Omega_i}{\omega}\right)^2\mathrm{Re}(E_z\partial_z(E_p^* e^{-i\xi})), \tag{18}$$

$$\langle F\rangle_{ey}\rightarrow m\left(\frac{M}{m}\right)^2\left(\frac{c}{B_0}\frac{\Omega_i}{\omega}\right)^2 2\,\mathrm{Re}(E_z^*\partial_z E_y), \tag{19}$$

$$\langle F\rangle_{ez}\rightarrow 2m\frac{M}{m}\frac{c^2}{B_0^2}\frac{\Omega_i}{\omega}\mathrm{Im}(\partial_z(E_p^* e^{-i\xi}E_y)), \tag{20}$$

$$\langle u\rangle_{ex}\rightarrow 2\left(\frac{M}{m}\right)\frac{c^2}{B_0^2}\frac{\Omega_i}{\omega^2}\mathrm{Re}(E_z^*\partial_z E_y), \tag{21}$$

$$\langle u\rangle_{ey}\rightarrow 2\left(\frac{M}{m}\right)\frac{c^2}{B_0^2}\frac{\Omega_i}{\omega^2}\mathrm{Re}(E_z\partial_z(E_p^* e^{-i\xi})). \tag{22}$$

The particular scaling used in Eqs. (18)–(22) and the mass ratio M/m has been introduced because it is useful in comparing the electron force and flow components with the ion force and flow components. Because the electrons have no significant polarization velocity, the perpendicular force terms for the electrons are due to the $\mathrm{Re}(-e\tilde{\mathbf{v}}_{ez}^*\times\tilde{\mathbf{B}}/c)$ force. In the y direction, the force on the electrons is then $\mathrm{Re}(e\tilde{v}_{ez}^*\tilde{B}_x/c)$, and, since there is no magnetic field component of the pump wave in the x direction, the largest ponderomotive force term for the electrons in the y direction does not depend on the beat with the pump wave amplitude. However, in the x direction the force acting on the electrons is $\mathrm{Re}(-e\tilde{v}_{ez}^*\tilde{B}_y/c)$, and, since the pump wave does have a magnetic field component in the y direction, the largest ponderomotive force term for the electrons in the x direction does depend on the beat with the pump wave amplitude.

For ions, the largest terms of the ponderomotive force and drift-velocity components are

$$\langle F\rangle_{ix}\rightarrow 2M\frac{c^2}{B_0^2}\mathrm{Re}(E_p^* e^{-i\xi}\partial_y E_y), \tag{23}$$

$$\langle F\rangle_{iy}\rightarrow -2M\frac{c^2}{B_0^2}\mathrm{Re}(E_p^* e^{-i\xi}\partial_x E_y), \tag{24}$$

$$\langle F\rangle_{iz}\rightarrow -2M\frac{c^2}{B_0^2}\frac{\Omega_i}{\omega}\mathrm{Im}(\partial_z(E_p^* e^{-i\xi}E_y)), \tag{25}$$

$$\langle u\rangle_{ix}\rightarrow -2\frac{c^2}{B_0^2}\frac{1}{\Omega_i}\mathrm{Re}(E_p^* e^{-i\xi}\partial_x E_y), \tag{26}$$

$$\langle u\rangle_{iy}\rightarrow 2\frac{c^2}{B_0^2}\frac{1}{\Omega_i}\mathrm{Re}(E_p^* e^{-i\xi}\partial_y E_y). \tag{27}$$

A. Axial ponderomotive force

The expressions given for $\langle F\rangle_{ez}$ and $\langle F\rangle_{iz}$ in Eqs. (20) and (25) are equal and opposite, hence the total force on the bulk plasma due to these terms is zero. In order to find the largest parallel force acting on the bulk plasma, not just the largest parallel force on the individual species, it is necessary to find the next largest parallel force term acting on the electrons and ions. The force terms which actually affect the bulk-plasma response are

$$\langle F\rangle_{ez}\rightarrow -m\frac{c^2}{B_0^2}\left\{\frac{M^2}{m^2}\frac{\Omega_i^2}{\omega^2}\partial_z|E_z|^2\right\} \tag{28}$$

and

$$\langle F\rangle_{iz}\rightarrow M\frac{c^2}{B_0^2}\{2\,\mathrm{Re}[\partial_z(E_p^* e^{-i\xi}E_x)]\}. \tag{29}$$

To provide a useful expression in terms of the relevant physical parameters that control the interaction of a large-scale Alfvén wave with a density perturbation, Eqs. (28) and (29) are expressed in terms of the scaled axial and transverse electric fields η_z, η_x [as defined in Eqs. (17)–(19) in Ref. 8] and the scaled axial distance $\xi=\omega z/v_A$,

$$\langle F\rangle_{ez}\rightarrow -\frac{1}{8}\left(\frac{\delta n}{n_0}\right)^2 l_\parallel^2 l_\perp^4(M\omega v_A)\left(\frac{B_p}{B_0}\right)^2\left(\frac{k_s}{k_A}\right)^2\partial_\xi|\eta_z|^2, \tag{30}$$

$$\langle F\rangle_{iz}\rightarrow \frac{1}{\sqrt{2}}\left(\frac{\delta n}{n_0}\right) l_\parallel l_\perp^2(M\omega v_A)\left(\frac{B_p}{B_0}\right)^2\mathrm{Re}[\partial_\xi(e^{-i\xi}\eta_x)], \tag{31}$$

where $l_\parallel=k_A L_\parallel$, and $l_\perp=k_s L_\perp$ are the scaled axial and transverse scale lengths of a Gaussian density perturbation having fractional amplitude $\delta n/n_0$, with $k_A=\omega/v_A$ and k_s

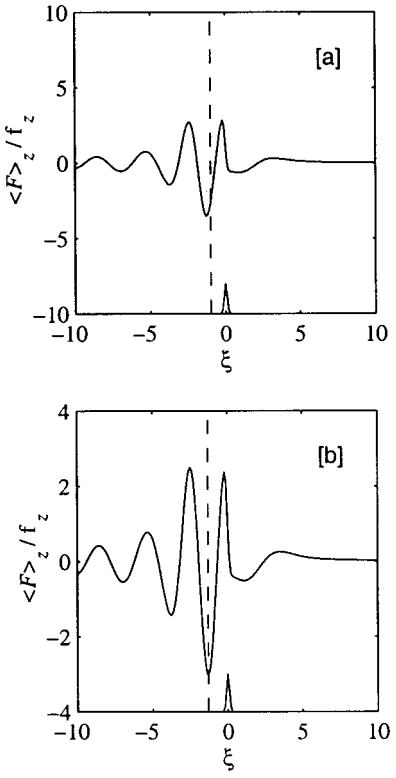

FIG. 2. Axial dependence of the total, scaled parallel ponderomotive force: (a) at ($k_s x=0$, $k_s y=0$), and (b) at ($k_s x=0$, $k_s y=0$). The dashed line marking the peak parallel force is located at $\xi=-1$ for (a) and at $\xi=-1.3$ for (b). The solid bump at the bottom corresponds to $\delta\tilde{n}$. The scaling factor f_z is given by Eq. (33).

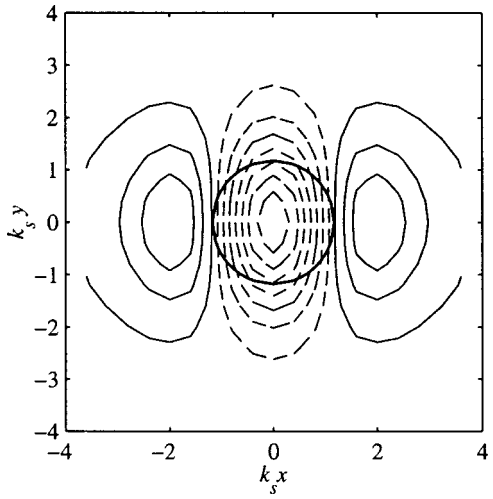

FIG. 3. Transverse dependence of the total, scaled parallel ponderomotive force at fixed axial position $\xi=-1$. The dashed contours of constant force value indicate a negative parallel force and the solid contours indicate a positive parallel force. The dark circle in the center corresponds to where $\delta\tilde{n}$ achieves one-half its peak value. To be compared with Fig. 2.

$=\omega_{pe}/c$. The amplitude of the magnetic field of the large-scale Alfvén wave is B_p and B_0 is the magnitude of the confining magnetic field.

For a typical scenario in which $l_\parallel=0.1$, $l_\perp=1.0$, $c/v_A=100$, $k_s/k_A\sim 10^3$, as examined in detail in Ref. 8, the scaled fields exhibit gradient terms such that $\partial_\xi|\eta_z|\sim 3\times 10^{-3}$, $\partial_\xi|\eta_x|\sim 2$ thus implying that for $\delta n/n_0\sim 0.1$ (as might be encountered in a perturbed plasma) the parallel ponderomotive force acting on the ions is approximately 100 times larger than that acting on the electrons. Thus, for situations of relevance to this transformation process, the bulk force giving rise to axial density rearrangements is dominated by the ion nonlinearity. As is seen from Eq. (31), the relevant modifications are thus proportional to the amplitude of the seed perturbation $\delta n/n_0$, depend on the square of the fractional magnetic field fluctuation $(B_p/B_0)^2$, and are spatially nonlocal because they arise from the beat between two signals over an extended region away from the location of the seed perturbation that triggers the nonlinear process.

The axial dependence of the bulk-plasma ponderomotive force along the ambient magnetic field is shown in Figs. 2(a) and 2(b) for two different transverse locations, ($k_s x=0$, $k_s y=0$) and ($k_s x=0.8$, $k_s y=0.8$). The origin of the coordinate system ($x=0$, $y=0$) refers to the center of the seed density perturbation having the form

$$\delta\tilde{n}(x,y,z)=\delta n\exp\left(-\frac{(x^2+y^2)}{2L_\perp^2}-\frac{z^2}{2L_\parallel^2}\right), \tag{32}$$

used to determine the scaled fields η_x, η_y, η_z.

The magnitude of the bulk force shown in Figs. 2(a) and 2(b) is scaled to the natural scaled force for this problem, namely

$$f_z=\frac{1}{\sqrt{2}}\left(\frac{\delta n}{n_0}\right)\left(\frac{B_p}{B_0}\right)^2(M\omega v_A), \tag{33}$$

and the scaled fields have been evaluated for $l_\perp=1.0$ and $l_\parallel=0.1$.

As seen from Figs. 2(a) and 2(b), the axial ponderomotive force is largest to the left of the seed perturbation and exhibits changes in sign. A consequence of this behavior is that on a longer time scale an extended density structure consisting of density depletions and enhancements can develop away from the seed perturbation. The nonlinear density modifications also experience a nonlocal character in the direction transverse to the confining magnetic field, as can be deduced from the transverse spatial pattern of the parallel bulk force in the (x,y) plane, shown in Fig. 3. The force in Fig. 3 is measured at axial position $\xi=-1$. The dark circle in the middle corresponds to where the seed perturbation $\delta\tilde{n}$ achieves one-half of its peak value. The contours surrounding this circle represent constant values of the axial ponderomotive force [scaled by f_z given by Eq. (33)] acting on the bulk plasma. The solid lines correspond to positive values and the dashed lines correspond to negative values. The positive contours range from ~ 0.2 to ~ 1.8 and the negative contours range from ~ -0.6 to ~ -5.5. The axial forces exhibit nonlocal behavior arising away from the center of the seed perturbation, as can be seen in Fig. 3 for $|k_s x|\geqslant 2$, and are associated with the transverse spreading of the short-scale field along the cone angle. The characteristic azimuthal variation is a consequence of the dipole-like, *in situ* antenna.

Although a proper assessment of the density rearrangement and plasma structuring that results from the axial ponderomotive force requires the numerical solution of a three-

dimensional, magnetized density evolution equation, it is useful to identify a characteristic scaling that indicates when the nonlinear effects addressed in this study play a significant role.

As mentioned earlier, the bulk-plasma ponderomotive force is essentially given by Eq. (31) and implies a force density

$$\langle \mathcal{F}_z \rangle \rightarrow n_0 f_z \, \mathrm{Re}[\partial_\xi (e^{-i\xi} \eta_x)], \tag{34}$$

with which it is useful to associate a pseudopotential Φ, such that $\langle \mathcal{F}_z \rangle = \partial \Phi / \partial z$. To estimate the conditions under which significant nonlinear density modifications may arise, this pseudopotential is to be compared to the electron plasma pressure. Hence, the useful scaled quantity that controls this process is

$$\frac{\max(\Phi)}{n_0 T_e} = \sqrt{2} l_\parallel l_\perp^2 \left(\frac{\delta n}{n_0} \right) \left(\frac{B_p}{B_0} \right)^2 \frac{1}{\beta_e} \max[\mathrm{Re}(e^{-i\xi} \eta_x)], \tag{35}$$

where $\beta_e = 8\pi n_0 T_e / B_0^2$ is the thermal to magnetic energy ratio and T_e is the electron temperature. From Eq. (35), it can be deduced that significant density modifications associated with the magnetic field B_p of the primary large-scale wave satisfies the requirement $B_p / B_0 > 9\sqrt{\beta_e}$ for $l_\parallel l_\perp^2 (\delta n / n_0) \approx 10^{-2}$.

B. Nonlinear drifts

Next we consider the nonlinear drifts associated with the scale transformation process. As seen from Eq. (21), in the x direction the electron drift is solely due to the secondary small-scale waves, hence it is smaller by a factor of $\delta n / n_0$ than the electron drift velocity in the y direction. For the ions, however, the drifts in both the x and y directions arise due to the beat between the pump wave and the secondary wave.

Using the same scaling procedure applied to the axial ponderomotive force (i.e., in terms of the scaled fields η_x, η_y, η_z) extracts the relevant scaling quantity associated with the nonlinear drifts, namely

$$v_{\mathrm{NL}} = \frac{1}{\sqrt{2}} \sqrt{\frac{M}{m}} v_{\mathrm{A}} l_\parallel l_\perp^2 \left(\frac{\delta n}{n_0} \right) \left(\frac{B_p}{B_0} \right)^2. \tag{36}$$

With this scaling, the ion drifts take the simple form

$$\langle u \rangle_{ix} \rightarrow - v_{\mathrm{NL}} \, \mathrm{Re}[e^{-i\xi} \partial_{x_s} \eta_y], \tag{37}$$

$$\langle u \rangle_{iy} \rightarrow v_{\mathrm{NL}} \, \mathrm{Re}[e^{-i\xi} \partial_{y_s} \eta_y], \tag{38}$$

where $x_s \equiv k_s x$ and $y_s \equiv k_s y$.

For the electrons, the relevant expression is

$$\langle u \rangle_{ey} \rightarrow v_{\mathrm{NL}} \sqrt{\frac{M}{m}} \frac{\Omega_i}{\omega} \mathrm{Re}[\eta_z \partial_\xi e^{-i\xi}]. \tag{39}$$

As can be deduced from Eqs. (37) and (38), for the ions the magnitude of the x and y components of the drift velocity are comparable. The electron drift, however, is essentially unidirectional and has a scaling that differs from the ion drifts by the large factor $(M/m)^{1/2}(\Omega_i / \omega)$. However, the electron term is driven by the scaled parallel electric field, η_z, which is smaller than η_y by roughly the same factor. Consequently, the magnitude of the nonlinear drifts experienced by electrons and ions is comparable, but exhibit a different spatial pattern.

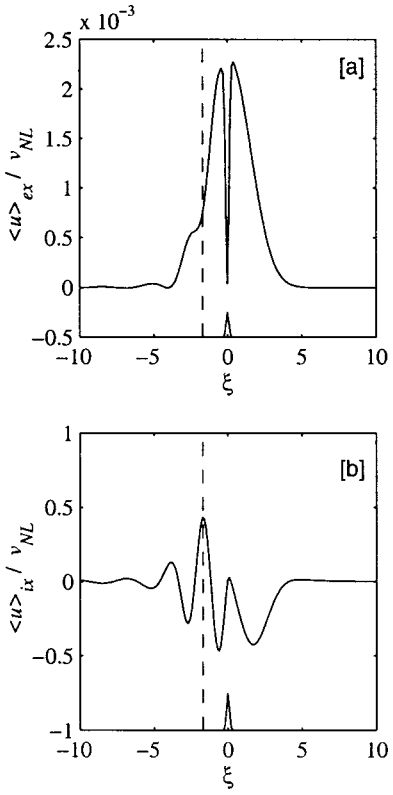

FIG. 4. Axial dependence of the scaled electron drift velocity in the x direction: (a) at ($k_s x = 0.8$, $k_s y = 0.8$), and (b) at ($k_s x = 0.8$, $k_s y = 0.8$). The solid bump at the bottom corresponds to $\delta \tilde{n}$. The dashed line marks the position of maximum ion drift velocity at $\xi = -1.7$. v_{NL} is given by Eq. (36).

The axial dependence of the scaled nonlinear drifts in the x direction at a position ($k_s x = 0.8$, $k_s y = 0.8$) is shown for the electrons in Fig. 4(a) and for the ions in Fig. 4(b). The transverse electron drift in Fig. 4(a) is scaled to v_{NL} in order to compare it directly to the ion drift. Evidently, for the x direction the ion flow dominates. As in the case of the axial ponderomotive force shown in Figs. 2(a) and 2(b), the nonlinear ion flows are larger to the left of the seed perturbation since they are dominated by the interference between the large- and small-scale waves.

Figures 5(a) and 5(b) display the axial dependence of the scaled electron and ions drifts in the y direction for a transverse position ($k_s x = 0.8$, $k_s y = 0.8$). The scaling is as in Fig. 4. It is seen from Fig. 5 that in the y direction the electron and ion drifts are comparable and both are larger to the left of the seed perturbation since they both arise from the interference pattern.

The transverse flow pattern for the electrons is shown in Fig. 6(a) at an axial position $\xi = -1.7$ corresponding to the dashed lines in Figs. 4 and 5. The transverse flow pattern of the ions at the same axial position is shown in Fig. 6(b). As in Fig. 3, the inner dark circle in the center represents the location where $\delta \tilde{n}$ achieves half of its maximum value. For ease of viewing, the arrows in the ion flow pattern are mul-

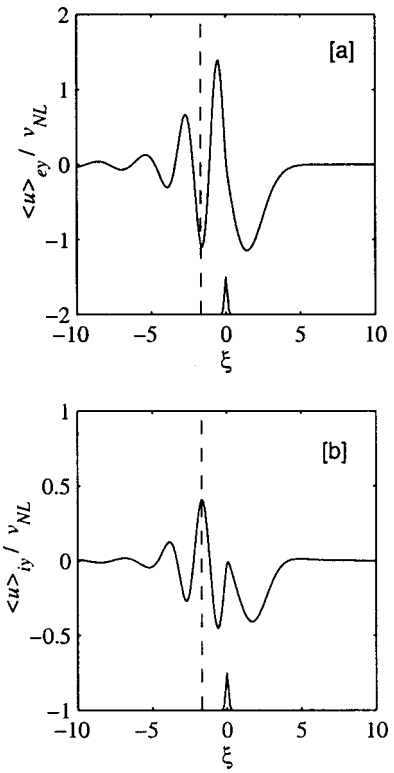

FIG. 5. Axial dependence of the scaled drift velocity in the y direction at $(k_s x = 0.8,\ k_s y = 0.8)$ for electrons (a) and ions (b). The solid bump at the bottom corresponds to $\delta\tilde{n}$. The dashed line marks the position of maximum ion drift velocity at $\xi = -1.7$.

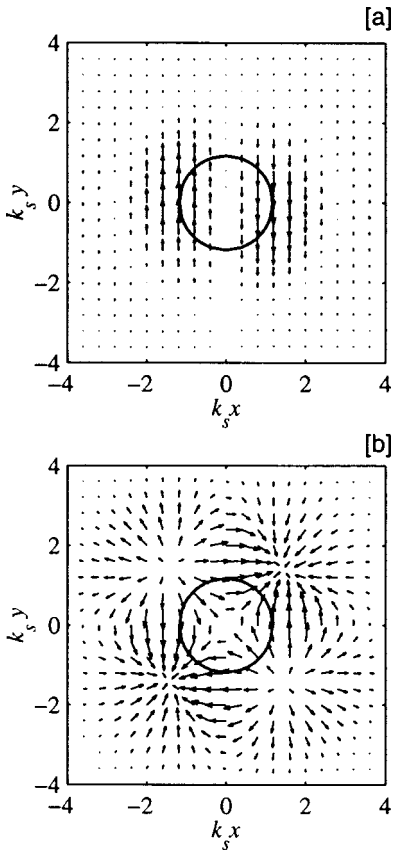

FIG. 6. The transverse flow pattern at the axial position $\xi = -1.7$ for electrons (a) and ions (b). For ease of viewing, the ion flow pattern is multiplied by a factor of 2 compared to the electron flow pattern. The dark circle in the center corresponds to the contour where $\delta\tilde{n}$ is one-half its peak value.

tiplied by a factor of 2 compared to those in the electron flow. It is seen that the ion flow exhibits an $l = 2$ azimuthal pattern with apparent sources and sinks outside the seed perturbation. The electrons flow essentially between these source/sink regions along the y direction, which is in the same direction as the oscillatory $E \times B$ drift associated with the large-scale wave.

The unusual transverse pattern exhibited by the nonlinear drifts displayed in Fig. 6 is a direct consequence of the topology of the electric field components of the small-scale wave. To help visualize the cause of the flow pattern, Fig. 7(a) displays the magnitude of the parallel component E_z and Fig. 7(b) displays the magnitude of the E_y component. As is seen from Eq. (39), the electron flow pattern is determined by η_z (scaled E_z), which in Fig. 7(a) is seen to peak slightly outside the seed perturbation and to be elongated along the y direction. It is worth emphasizing that this E_z is responsible for sustaining the two self-consistent, field-aligned current channels of opposite polarity that support the magnetic field associated with the small-scale wave. A nonlinear consequence of driving the opposite polarity axial currents is to develop dc flows, also of opposite polarity, across the magnetic field.

As follows from Eqs. (37) and (38), the transverse ion drifts are determined by the transverse gradients in the quantity η_y (scaled E_y). From Fig. 7(b), it is seen that E_y exhibits an $l = 2$ azimuthal variation that gives rise to the corresponding $l = 2$ flow pattern, including the sinks and sources displayed in Fig. 6.

As in the discussion of the axial ponderomotive force, it is useful to establish a condition that indicates when the dc flows become significant. In this case, the relevant parameter is the ion sound speed $c_s = \sqrt{T_e/M}$. Using the natural scale of the transverse flows given by Eq. (36) results in the ratio

$$\frac{v_{\mathrm{NL}}}{c_s} = \sqrt{\frac{M}{m}}\, l_{\parallel} l_{\perp}^2 \left(\frac{\delta n}{n_0}\right)\left(\frac{B_p}{B_0}\right)^2 \frac{1}{\sqrt{\beta_e}}, \tag{40}$$

from which it can be deduced that modifications produced by nonlinear flows are expected to become prominent when the magnetic field of the large-scale wave satisfies the requirement $B_p/B_0 > 10(\beta_e m/M)^{1/4}$.

It is noteworthy that in general the transverse dc flow patterns exhibited by the electrons and ions do not give rise to net current cancellation. In fact, Fig. 8 displays the net current density vector $\mathbf{j} = e(n_0 + \delta\tilde{n})(\mathbf{u}_i - \mathbf{u}_e)$ at an axial position $\xi = -1.7$, corresponding to Figs. 6 and 7. Of course, the pile-up of charge suggested by Fig. 8 implies that additional axial dc currents must arise to close the circuit. The consequence of this circuit is that an axial dc-magnetic field develops out of the scale transformation process. It should be mentioned that recent studies[17–19] based on kinetic descriptions and two-fluid magnetohydrodynamics have investigated in detail the analogous problem of poloidal flow generation by radio frequency waves in tokamak plasmas. In one of the studies[17] it is also found that nonambipolar cross-field

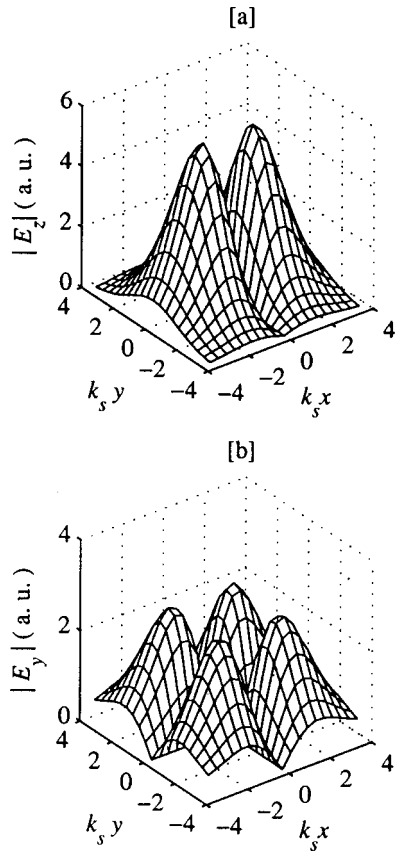

FIG. 7. (a) Transverse spatial dependence of the magnitude of the axial electric field. (b) Transverse spatial dependence of the magnitude of E_y. Both are at a fixed axial position $\xi=-1.7$.

transport arises from the wave nonlinearities. In Fig. 8 the additional contribution to the time-averaged nonlinear current from the term $\langle \delta\tilde{n}\tilde{v}_\perp \rangle$ is not included because it is smaller by the factor ω/Ω_i. The physical reason is that $\delta\tilde{n}$ is typically very small for the shear Alfvén waves of interest.

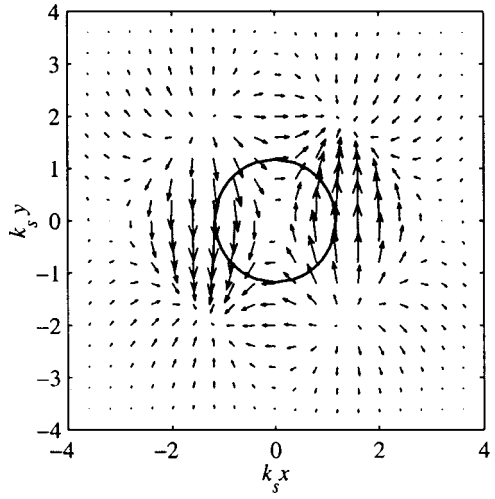

FIG. 8. Transverse current density pattern $e(n_0+\delta\tilde{n})(\mathbf{u_i}-\mathbf{u_e})_\perp$ at an axial position $\xi=-1.7$. The dark circle in the center corresponds to the contour where $\delta\tilde{n}$ is one-half its peak value.

IV. STREAMING INSTABILITIES

A significant feature of the scale transformation process is the spontaneous development of axial electric fields E_z that drive the two field-aligned current channels of opposite polarity. For extreme conditions, it is possible that the axial electron drift velocities associated with the current channels exceed the threshold to drive axial streaming instabilities, e.g., the ion acoustic instability or, for large values of the electron drift, the Buneman instability. The purpose of this section is to survey the relevant properties of such streaming instabilities and to relate those results to the scale transformation scenario.

For simplicity, in this limited study of the streaming instabilities, we survey only the ideal case of a uniform plasma for zero transverse wave number (i.e., $k_\perp=0$). Several interesting features arise when transverse gradients of the streaming parameters are included,[20] but their study requires substantial and lengthy analysis, which is beyond the scope of the present paper.

The linear dispersion relation appropriate for a collisionless plasma in which the ion distribution function is a Maxwellian with temperature T_i and the electron distribution function is a Maxwellian with temperature T_e, but having an axial drift velocity V_D relative to the ion species, is

$$0=1-\frac{\omega_{pi}^2}{2v_{T_i}^2k_z^2}Z'\left(\frac{\omega}{\sqrt{2}k_z v_{T_i}}\right)-\frac{\omega_{pe}^2}{2v_{T_e}^2k_z^2}Z'\left(\frac{\omega-k_zV_D}{\sqrt{2}k_z v_{T_e}}\right), \tag{41}$$

where $v_{T_e}=\sqrt{T_e/m}$, $v_{T_i}=\sqrt{T_i/M}$, and Z' is the derivative of the familiar plasma dispersion function.[21]

Due to the geometry in which the streaming instabilities arise during the scale transformation process, it is appropriate to examine the ''spatial problem'' rather than the more frequently discussed ''initial value problem.''[22] This implies that we seek roots of Eq. (41) in which k_z is complex and the corresponding wave frequency ω is a real quantity (determined by ambient noise fluctuations). The natural scaling of k_z is the electron Debye wave number $k_{De}=\omega_{pe}/v_{T_e}$, from which it follows that the properties of the relevant instabilities are controlled by the two scaled parameters V_D/v_{T_e} and T_e/T_i, with ω/ω_{pi} the independent variable, where ω_{pi} is the ion plasma frequency.

The frequency dependence of the imaginary part of k_z, obtained from numerical solutions of Eq. (41), is shown in Fig. 9(a) for an electron to ion temperature ratio of $T_e/T_i=1.0$ and in Fig. 9(b) for $T_e/T_i=10$. The various solid curves correspond to different values of V_D/v_{T_e}. In the notation used, a spatially growing signal corresponds to $\mathrm{Im}(k_z)<0$. As expected, Fig. 9(a) indicates that for $T_e/T_i=1$ substantial electron drifts are required to trigger the spatial amplification of the ambient noise. A feature of relevance to observation on board of spacecraft and in the laboratory is that over a broad range of conditions sampled in Fig. 9(a) the signals that experience the largest growth have a frequency in the neighborhood of $\omega/\omega_{pi}\sim 0.5$.

The frequency dependence of the real part of k_z is shown in Fig. 10(a) for $T_e/T_i=1$ and in Fig. 10(b) for $T_e/T_i=10$. It

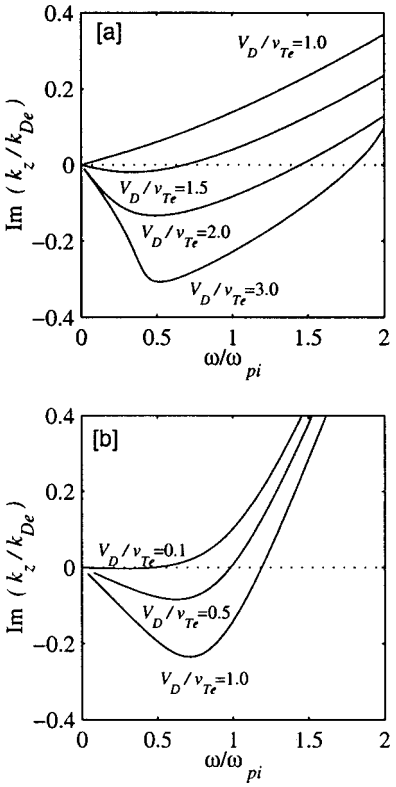

FIG. 9. Frequency dependence of the imaginary part of the parallel wave number for various drift velocities when (a) $T_e/T_i=1$ and (b) $T_e/T_i=10$.

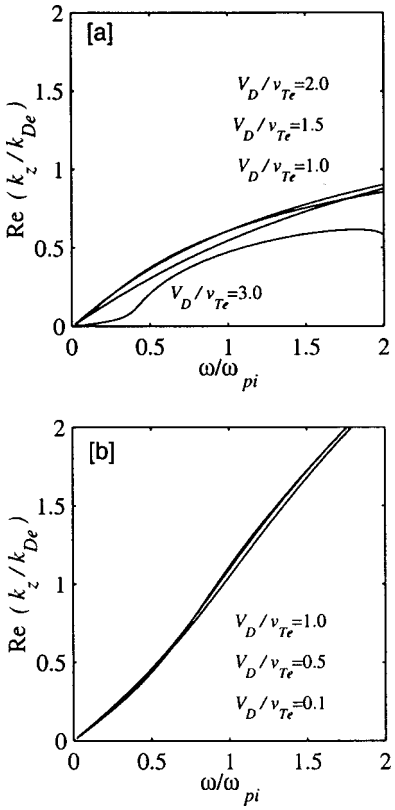

FIG. 10. Frequency dependence of the real part of the parallel wave number for various drift velocities when (a) $T_e/T_i=1$ and (b) $T_e/T_i=10$.

is seen from Figs. 10(a) and 10(b) that the value of T_e/T_i is more significant than the value of V_D/v_{T_e} in determining the topology of Re(k_z). The effective phase velocity of the fastest growing modes shown in Figs. 9 and 10 is found to be slightly larger than c_s and increases as V_D/v_{T_e} increases. For $V_D/v_{T_e}=3$, $\omega/\mathrm{Re}(k_z)\simeq 2.5c_s$ and the mode transitions into the Buneman instability.

Since the frequency ω of the modes driven unstable is much larger than the frequency ω_0 of the Alfvén structures, the spatial growth rates can be deduced from the instantaneous axial drift velocity resulting from E_z. In terms of the quantities of relevance to the scale transformation process the scaled drift parameter takes the form

$$\frac{V_D}{v_{T_e}}=\mathcal{A}_v\{\mathrm{Im}(\eta_z)\cos(\omega_0 t+\phi)-\mathrm{Re}(\eta_z)\sin(\omega_0 t+\phi)\}, \tag{42}$$

where ϕ is the wave phase and the scaled axial fields η_z depend on position. The quantity that determines when the streaming instabilities are of significance is

$$\mathcal{A}_v=\frac{1}{2}\left(\frac{\Omega_i}{\omega_0}\right)\left(\frac{\delta n}{n_0}\right)l_\parallel l_\perp^2\left(\frac{B_p}{B_0}\right)\sqrt{\frac{M}{m}\frac{1}{\beta_e}}. \tag{43}$$

From results such as those shown in Figs. 9(a) and 9(b), it is possible to determine the threshold value of V_D/v_{T_e} required to cause spatial amplification of a noise fluctuation at frequency ω. Furthermore, from the self-consistent calculation of the field structures the scaled fields η_z are known, thus it is possible to deduce what values of $\mathcal{A}_v$ are required to trigger the streaming instabilities. For example, it is found that for $\omega/\omega_{pi}=0.1$ a value of $\mathcal{A}_v\sim 100$ is necessary for $T_e/T_i=1$, while for $T_e/T_i=10$ the threshold is reduced to $\mathcal{A}_v\sim 10$.

Figure 11 illustrates the situation that may be sampled by a spacecraft or in a laboratory experiment where the scale transformation process is present. The spatial dependence of the imaginary part of k_z for a noise frequency of $\omega/\omega_{pi}=0.1$ is displayed in Fig. 11. The solid curves represent the

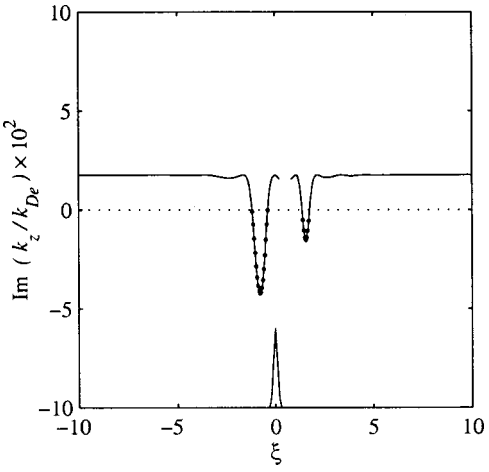

FIG. 11. Axial dependence of the imaginary part of the parallel wave number. $T_e/T_i=1$ and $\omega/\omega_{pi}=0.1$. The dark overlayed data points indicate regions of instability. The solid bump at the bottom corresponds to $\delta\tilde{n}$. The transverse position is ($k_s x=1$, $k_s y=0$).

continuous spatial variation including regions where the mode is damped and regions where the mode grows. The growing mode regions [i.e., areas where $\mathrm{Im}(k_z)<0$] are represented by the heavy dots. The solid bump at the bottom of the panels corresponds to the seed perturbation $\delta\tilde{n}$. The transverse spatial location is $(k_s x=1, k_s y=0)$. This case corresponds to $T_e/T_i=1$ and $\mathcal{A}_v=100$. The snapshot presented is for a phase factor $\omega_0 t+\phi=2\pi$ in Eq. (42). Clearly, as time progresses, the instabilities are shut-off and reappear half a period later (i.e., they grow when E_z points right or left). Analogous results are obtained for $T_e/T_i=10$ at the lower value of $\mathcal{A}_v=10$ and, for the sake of brevity, are not shown in this work.

As is seen from Fig. 11, regions of significant wave activity can develop from this process at remote locations from the seed perturbation. As the unstable waves grow, they can give rise to electron acceleration and ion heating, depending on how large B_p/B_0 is.

It is useful to estimate at what levels of B_p/B_0 the streaming instabilities become important in the stringent environment of a $T_e/T_i=1$ plasma. For the conditions associated with Figs. 10(a) and 10(b), and considering a typical scenario with $\Omega_i/\omega_0=10$, $\sqrt{M/m}\simeq 40$, $l_\parallel=0.1$, $l_\perp=1$, $\delta n/n_0=10^{-1}$, results in

$$\frac{B_p}{B_0}>50\sqrt{\beta_e}. \tag{44}$$

V. CONCLUSIONS

This study has considered three major nonlinearities that arise when a propagating, large-scale Alfvén wave encounters an ambient, filamentary density perturbation in a low-β plasma. The motivation for this investigation is the need to identify a general mechanism that allows for the transfer of the energy content in large-scale Alfvén waves to plasma particles and the subsequent development of plasma structures with embedded high-frequency noise. This is a situation which is increasingly being observed by rockets[23] and spacecraft[24] and which may also be accessible to laboratory studies.

The nonlinearities explicitly considered in this work are the ponderomotive force, the generation of dc drifts, and the triggering of axial streaming instabilities. An important companion nonlinearity, namely instabilities driven by shear flows,[25] has been explicitly left out. The reason is that such a study requires lengthy, specialized techniques whose clear exposition deserves a dedicated manuscript. Nevertheless, it must be recognized that such a process can play a dominant role in certain environments of interest.

A general expression has been given by Eq. (7) for the fluid ponderomotive force acting on individual cold plasma species. For future reference, no approximations have been made concerning the structure of the fields (e.g., wave packets or slab geometry). The results have been expressed in three dimensions in terms of the individual components of the complex amplitude of the electric field. For clarity, and to avoid existing controversies in the field, the origin of each term has been explicitly identified. A simple expression for the axial ponderomotive force acting on an individual cold fluid plasma species is given in Eq. (8) for the relevant limit of a field structure in the shear-Alfvén-wave regime. In the appropriate limit, this expression is similar to that partially used by other investigators in recent studies.[12,13]

The general ponderomotive force of Eq. (7) has been explicitly evaluated for the fields associated with the scale transformation process. In this process, the primary large-scale wave interacts with an ambient density perturbation and radiates two, small-scale shear Alfvén waves. One wave propagates in the original direction of the large-scale wave and the other in the opposite direction. The total electric field consists of the interference of the primary wave with the secondary waves. Since terms in the ponderomotive force depend on the gradient of the total field, regions of partially standing waves play a dominant role. Because the amplitude of the secondary waves is proportional to $(\delta n/n_0)\times(B_p/B_0)^2$, where B_p is the fluctuating magnetic field amplitude of the primary wave and $\delta n/n_0$ the fractional amplitude of the seed perturbation, it is found that the relevant ponderomotive terms arise from the beat between the primary wave and the secondary waves, i.e., it is proportional to $(\delta n/n_0)(B_p/B_0)^2$.

The spatial structure of the ponderomotive force has been investigated (Figs. 2 and 3) and the salient feature is that nonlocal effects arise in regions remote from the seed perturbation. This implies that for sufficiently large amplitudes, this process can lead to global rearrangements of the ambient plasma density which ultimately may result in a turbulent medium of embedded density filaments.

In the direction transverse to the confining magnetic field, it is found that the ponderomotive force gives rise to unusual dc-flow patterns (Fig. 6) surrounding the seed perturbation. In general, the electron and ion flow patterns are spatially different and result in net dc currents (Fig. 8) that must eventually be compensated for by axial currents. In essence, the mechanism becomes a generator of dc magnetic fields.

A survey has been made of the axial streaming instabilities that can be triggered by the parallel electric fields associated with the short-scale secondary waves. Conditions have been obtained for the onset of spatially growing noise. As in the case of the ponderomotive force, regions of spontaneous wave activity can develop away from the location of the seed perturbation. The growing high-frequency noise can give rise to ion heating and formation of structures in the electron distribution function having axial scale lengths on the order of the Debye length.

The effectiveness of the three nonlinear processes has been summarized in terms of useful scaled parameters. The density rearrangements are regulated by Eq. (35), the dc flows by Eq. (36), and the streaming instabilities by Eq. (43). All the scaled parameters depend linearly on the properties of the seed perturbation through the factor $l_\parallel l_\perp^2(\delta n/n_0)$. Therefore, it is possible to assess the relative importance of the three nonlinear mechanisms as the amplitude of the primary wave is increased. For realistic estimates of $l_\parallel l_\perp^2(\delta n/n_0)$, the ponderomotive density changes become

significant for $B_p/B_0 > 9\sqrt{\beta_e}$, the dc drifts for $B_p/B_0 > 10(\beta_e m/M)^{1/4}$, and the streaming instabilities for $B_p/B_0 > 50\sqrt{\beta_e}$. It is, of course, assumed throughout this study that the condition $\beta_e \ll m/M$ prevails. From these inequalities it can be deduced that as B_p/B_0 is increased the first changes that should occur are density modifications, and as B_p/B_0 is increased further the streaming instabilities are activated. Thus, at large levels of the pump wave amplitude, a scenario arises in which high-frequency noise and density modifications develop simultaneously. Significant dc flows and associated current loops also appear, but they are expected to develop in a noisy environment in which large changes in the ambient conditions are taking place.

It should be noted that throughout this manuscript the parameters of the primary wave have been held constant. If situations encountered in space or laboratory environments lead to the generation of substantial nonlinear density modifications or particle heating, care must be taken not to extrapolate the formulas presented, since pump modification must accordingly be incorporated in the calculations.

In summary, a study of nonlinear effects associated with the interaction between a large-scale Alfvén wave and a seed density perturbation indicates that this process causes the development of density structures and high frequency noise in low-β plasmas. The secondary noise in turn can lead to ion heating and the formation of distortions in the electron distribution functions.

ACKNOWLEDGMENTS

This work is sponsored by the Office of Naval Research and the U.S. Department of Energy.

[1] C. A. Kletzing, J. Geophys. Res. **99**, 11095 (1994).
[2] A. V. Streltsov and W. Lotko, J. Geophys. Res. **100**, 19457 (1995).
[3] I. Roth and M. Temerin, Astrophys. J. **477**, 940 (1997).
[4] A. F. Viñas, H. K. Wong, and A. J. Klimas, Astrophys. J. **528**, 509 (2000).
[5] J. R. Wygant, A. Keiling, C. A. Cattel, M. Johnson, R. L. Lysak, M. Temerin, F. S. Mozer, C. A. Kletzing, J. D. Scudder, W. Peterson, C. T. Russel, G. Parks, M. Brittnacher, G. Germany, and J. Spann, J. Geophys. Res. **105**, 18675 (2000).
[6] J. E. Maggs and G. J. Morales, Phys. Plasmas **4**, 290 (1997).
[7] A. T. Burke, J. E. Maggs, and G. J. Morales, Phys. Plasmas **7**, 1397 (2000).
[8] T. Drozdenko and G. J. Morales, Phys. Plasmas **7**, 823 (2000).
[9] G. J. Morales, R. S. Loritsch, and J. E. Maggs, Phys. Plasmas **1**, 3765 (1994).
[10] P. M. Bellan, Phys. Plasmas **1**, 3523 (1994).
[11] W. Gekelman, D. Leneman, J. Maggs, and S. Vincena, Phys. Plasmas **1**, 3775 (1994).
[12] P. M. Bellan and K. Stasiewicz, Phys. Rev. Lett. **80**, 3523 (1998).
[13] P. K. Shukla and L. Stenflo, Phys. Plasmas **7**, 2738 (2000).
[14] P. K. Shukla and L. Stenflo, Phys. Rev. Lett. **85**, 2408 (2000); A. G. Elfimov and R. M. O. Galvao, *ibid.* **85**, 2409 (2000).
[15] W. Gekelman, P. Pribyl, N. Palmer, S. Vincena, and C. Mitchell, Bull. Am. Phys. Soc. **44**, 71 (1999), paper CP153.
[16] K. Stasiewicz, G. Holmgren, and L. Zanetti, J. Geophys. Res. **103**, 4251 (1998).
[17] L. A. Berry, E. F. Jaeger, and D. B. Batchelor, Phys. Plasmas **7**, 641 (2000).
[18] A. G. Elfimov, G. Amarante Segundo, R. M. O. Galvao, and I. C. Nascimento, Phys. Rev. Lett. **84**, 1200 (2000).
[19] J. R. Myra and D. A. D'Ippolito, Phys. Plasmas **7**, 3600 (2000).
[20] K. J. Reitzel and G. J. Morales, Phys. Plasmas **5**, 3806 (1998).
[21] B. D. Fried and S. D. Conte, *The Plasma Dispersion Function: The Hilbert Transform of the Gaussian* (Academic, New York, 1961).
[22] B. D. Fried and R. W. Gould, Phys. Fluids **4**, 139 (1961).
[23] K. L. McAdams, J. LaBelle, P. W. Schuck, and P. M. Kintner, Geophys. Res. Lett. **25**, 309 (1998).
[24] K. Stasiewicz, B. Holback, V. Krasnoselskikh, M. Boehm, R. Bostrom, and P. Kintner, J. Geophys. Res. **101**, 21515 (1996).
[25] G. Ganguli, Phys. Plasmas **4**, 1544 (1997).